Advanced Energy Materials

ADVANCED ENERGY MATERIALS
www.advenergymat.de

RESEARCH ARTICLE OPEN ACCESS

Nickel-Free Synthesis of Poly(pyrene-4,5,9,10-tetraone) for Sodium-based Batteries: Insights into Electrode Architecture and Reversible Na-ion Insertion

Md. Adil[1,2] | Robin Wessling[1,2] | Nico Kokott[1,2] | Elena Mena-Osteritz[1] | Benedikt Prifling[3] | Markus Osenberg[4] | Thomas Diemant[5] | Volker Schmidt[3] | Ingo Manke[4] | Birgit Esser[1,2,5]

[1]Institute of Organic Chemistry II and Advanced Materials, Ulm University, Ulm, Germany | [2]CELEST Green Energy Lab Ulm, Ulm University, Ulm, Germany | [3]Institute of Stochastics, Ulm University, Ulm, Germany | [4]Institute Electrochemical Energy Storage, Helmholtz-Zentrum Berlin für Materialien und Energie, Berlin, Germany | [5]Helmholtz Institute Ulm (HIU) Electrochemical Energy Storage, Ulm, Germany

Correspondence: Birgit Esser (birgit.esser@uni-ulm.de)

Received: 9 February 2026 | **Revised:** 28 April 2026 | **Accepted:** 13 May 2026

Keywords: conductive carbon architectures | green chemistry | organic batteries | polymer synthesis | sodium-metal batteries

ABSTRACT

Organic electrode-active materials offer a sustainable pathway toward sodium-based batteries, yet their application is hindered by electrolyte dissolution, limited conductivity, and synthetic challenges. Herein, we present an efficient nickel-free synthesis of poly(pyrene-4,5,9,10-tetraone) (PPTO), a high-capacity organic carbonyl-based polymer, via oxidative Pd-catalyzed homopolymerization of propylene glycol-protected PTO boronic esters. Among different conductive carbon-based electrodes, a PPTO@CNTs@Ketjen Black composite electrode achieves a reversible capacity of 286 mAh g^{-1} at 1 A g^{-1}, 72% capacity retention over 500 cycles, and delivers 201 mAh g^{-1} even at 10 A g^{-1}. An energy density of 549 Wh kg^{-1} (at low rates) and 346 Wh kg^{-1} (at high rates) is achieved based on active-material mass under half-cell conditions (275 Wh kg^{-1} based on total electrode mass). Ex situ spectroscopy, combined with theoretical calculations, reveals a two-electron redox process of each PTO unit with possible intermolecular interactions stabilizing the reduced state. Kinetic studies demonstrate rapid Na^+ transport ($D_{Na^+} \approx 10^{-10}$ cm^2 s^{-1}) and capacitive-dominated storage. Tomographic 3D image data reconstruction highlights the favorable microstructure of the CNT/Ketjen Black composite in hindering PPTO dissolution. This work provides insights into the interplay between polymer chemistry, electrode architecture, and ion transport, offering design principles for organic electrode materials for sodium-based batteries.

1 | Introduction

The global demand for sustainable and cost-effective energy storage devices has intensified the search for a viable alternative to lithium-ion batteries (LIBs) [1]. Among the emerging technologies, rechargeable sodium-ion batteries (SIBs) have garnered significant attention as a cost-effective and environmentally benign solution. Sodium has a widespread natural abundance and availability, in sharp contrast to lithium's limited and geographically concentrated reserves [2]. SIBs share many operational principles with LIBs, including similar intercalation chemistry. However, the large size of Na^+ (r = 1.02 Å) compared to Li^+ (r = 0.59 Å) introduces distinct challenges and opportunities for developing suitable electrode materials for applications demanding high cyclability and rate capability [3, 4].

Organic electrode-active materials (OAMs) are attractive candidates for SIB positive electrodes [5]. They offer a large portfolio

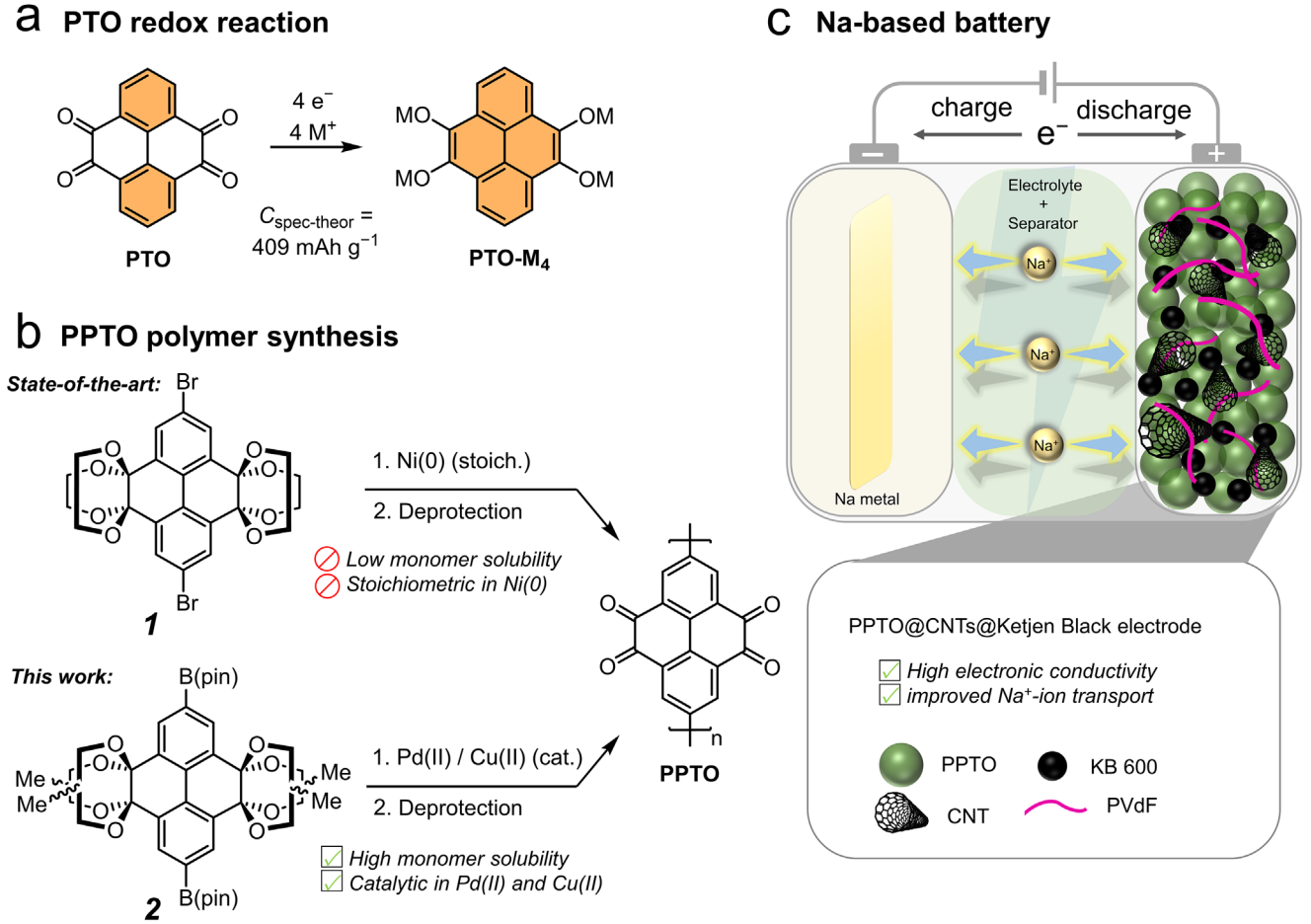

FIGURE 1 | Schematic illustration of the redox mechanism, polymer synthesis, and working principle of PPTO@CNTs@Ketjen Black electrodes for Na-based batteries. (a) Fourfold reduction of pyrene-4,5,9,10-tetraone (PTO) upon coordination of four monovalent cations (orange coloring indicates aromatic π-systems). (b) Synthetic route comparison for poly(PTO) (PPTO): previous Ni(0)-mediated polymerization with limited monomer solubility versus the present Pd(II)/Cu(II)-catalyzed oxidative cross-coupling of boronic ester monomers, offering improved solubility and catalytic efficiency. (c) Schematic of an Na-PPTO cell with optimized composite positive electrode incorporating carbon nanotubes and Ketjen Black carbon.

of diverse structures, have low toxicity, and can be produced from cost-effective and abundant raw materials [6, 7]. Often-used OAMs include carbonyl compounds [8, 9] or carboxylates [10] as n-type materials [11, 12], operating in a cation-rocking-chair configuration with reversible insertion of electrolyte cations, as well as p-type materials with quaternary nitrogen centers [13–18], or stabilized radicals [19]. The first type—namely conjugated carbonyl compounds—has attracted significant interest due to their multi-electron redox reactions, relatively high capacity and redox potential, and their ability to coordinatively bind metal cations in the discharged state [20, 21]. Pyrene-4,5,9,10-tetraone (PTO) stands out as a redox-active group with four carbonyl groups, enabling an up to fourfold reduction with the uptake of four monovalent metal ions (Figure 1a) [22]. This imparts PTO with a high theoretical specific capacity of 409 mAh g^{-1}. The driving force for the reduction of PTO is attributed to the additional aromaticity achieved in the tetraoxy-substituted anion (marked orange in Figure 1a).

PTO, as a small molecule, has been used as a redox-active group in OAMs on several occasions [23]. However, the high solubility of PTO in liquid battery electrolytes restricts its direct application as OAM. By using solid electrolytes, the dissolution can be suppressed, resulting in an improved cycling stability [24]. For example, Yao and coworkers fabricated a solid-state sodium-metal battery based on a PTO positive electrode using either the solid electrolyte Na_3PS_4, furnishing a high energy density (578 Wh kg^{-1}) and cycling stability [25] or a beta-alumina solid electrolyte, resulting in an even higher energy density of 900 Wh kg^{-1} [25, 26]. Alternatively, immobilization of the active material within a porous carbon matrix, combined with the application of a highly concentrated electrolyte, can also mitigate dissolution problems [21, 27]. A third strategy is to immobilize PTO in a carbon matrix through covalent bond linkage [28].

Besides these strategies, integrating redox-active organic moieties into polymeric structures has proven advantageous in lowering their solubility in liquid electrolytes [29]. The redox-active units can be incorporated into the main chain of the polymer or as a side group, i.e., of an insulating polymer backbone. The first strategy has the advantage that the density of redox-active groups in the polymer can be higher, and a lesser amount of inactive mass is introduced. Both strategies have been followed to incorporate PTO into polymers as well as into COFs or microporous polymers for application as OAM [30–43]. Due to the highest density of PTO groups and therefore highest theoretical specific capacity, the

linear homopolymer P(PTO), herein named PPTO for simplicity, is of particular relevance (Figure 1) [44]. Due to its low solubility and reactivity of the dione groups to basic conditions, PPTO is typically synthesized through metal-mediated in situ polymerization of an ethylene-glycol (EtG)-protected precursor in the presence of a carbon additive, which is a non-ideal procedure due to potential metal residues and for the scale-up of the synthesis [45–47]. Specifically, the literature synthetic route to PPTO involves a YAMAMOTO polymerization of EtG-protected dibromo-PTO **1**, employing an over-stoichiometric amount of bis(cycloocta-1,5-diene)nickel ($Ni(COD)_2$), that yields the EtG-protected polymer $P(PTO_{EtPG})$. This is then deprotected to give the target PPTO (Figure 1b) [44–46]. The main shortcoming of this approach is its low yield (38%, often no yield is reported) [44], which is mainly due to the poor solubility of the EtG-protected dibromo-PTO as monomer and the insolubility of the polymeric protected $P(PTO_{EtPG})$, leading to relatively short chain lengths being formed, and significantly complicating purification and analysis. The over-quantitative use of a nickel catalyst poses additional issues, as $Ni(COD)_2$ is comparatively expensive and difficult to handle (air-sensitivity) and has a negative impact on the overall life-cycle assessment of a potential battery application [48]. Second, nickel residues, which may be transferred over into later stages of the synthesis and into the active material, can potentially influence the electrochemical performance.

To alleviate these issues, we herein report a new synthetic pathway toward PPTO. The basis of this new approach is a new protecting-group strategy that we recently reported, using racemic propylene glycol (PrG, 1,2-propanediol) as a protecting group instead of ethylene glycol [49]. The extra methyl groups introduce regioisomerism and stereoisomerism into the molecule, which inhibits the tendency to crystallize and therefore drastically increases the solubility of the monomer. The increased solubility enabled us to develop a new polymerization method for PPTO using only catalytic amounts of palladium and copper, namely, an oxidative polymerization of boronic esters [50], which alleviates the heavy-metal-dependance of its synthesis.

We then use PPTO, accessed through the improved synthetic procedure, as electrode material in Na-based half cells (Figure 1c) while comparing various conductive carbon additives (Ketjen Black EC-600JD, Super P, SWCNTs (herein referred to as CNTs for simplicity)) along with two different electrode types (blade-coated on current collector vs. free-standing electrode). We find the best performance for the blade-coated PPTO electrode containing highly electrically conductive CNTs and mesoporous Ketjen Black EC-600JD (KB). The PPTO@CNTs@KB electrode delivers a specific capacity of 286 mAh g^{-1} at 1 A g^{-1} with 72% retention over 500 cycles, along with notable rate capability (201 mAh g^{-1} at 10 A g^{-1}). Using various characterization techniques, including X-ray photoelectron spectroscopy (XPS), Raman spectroscopy, and Fourier-transform infrared spectroscopy (FT-IR), electrode architecture engineering, tomographic 3D image data, as well as density-functional theory (DFT) calculations, we elucidate the sodium-ion insertion mechanism of the PPTO@CNTs@KB electrode. Overall, this work demonstrates a significantly improved synthetic route to PPTO as an attractive battery electrode material and—by conductive carbon optimization—sheds light onto its use as an electrode material for rechargeable organic-based sodium-metal batteries.

2 | Results and Discussion

2.1 | Synthesis and Characterization

Making use of the significantly increased solubility of PTO derivatives protected with propylene glycol [49], we first developed a new synthetic route to PPTO. As an alternative homopolymerization method to the YAMAMOTO coupling, we selected the oxidative homocoupling of boronic esters [50], a reaction initially optimized and mechanistically investigated for macrocycle synthesis [34, 51]. The corresponding synthetic route starting from bisborylated **2** is shown in Figure 2a [49]. We subjected **2** to polymerization conditions first developed by MINUS et al. [50]. The oxidative homocoupling uses $Pd(OAc)_2$ and $Cu(OAc)_2$ as co-catalysts, $B(OH)_3$ to prevent the peroxide-mediated decomposition of the boronic esters, and oxygen from the ambient (open vessel reaction) as the oxidant, and delivers the desired polymer $P(PTO_{PrG})$ with 52% yield. The open-vessel setup and the use of "wet" solvents make this polymerization method especially simple, practical, and scalable, and constitutes—next to avoiding the use of over-stoichiometric amounts of $Ni(COD)_2$— a significant advantage over the conventional YAMAMOTO polymerization.

Due to the use of propylene glycol as a protecting group, the resulting protected polymer $P(PTO_{PrPG})$ is well soluble in, e.g., tetrahydrofuran (THF), chloroform, and toluene. This facilitates a solution-based analysis of the protected polymer $P(PTO_{PrG})$. Not only can its purity be investigated by solution NMR spectroscopy (Figures S1 and S2, in addition to solid-state NMR, Figure S3), but the resulting molecular-weight distribution can be assessed via gel-permeation chromatography (GPC, Figure 2b). This analysis showed that the average degree of polymerization (X_n) achievable with this new approach is around 9.0, calculated from the number-average molecular weight ($\bar{M}_n = 4.41 \cdot 10^3$ g mol^{-1}). MALDI-MS detected the successful formation of a polymer with degrees of polymerization of 3–10 (Figure 2c). End-group analysis via ^1H NMR spectroscopy suggests an average degree of polymerization of $X_n \approx 12$ for $P(PTO_{PrG})$, even higher than that from the GPC or MALDI-MS measurement (Figure S4). We accredit this improvement compared to the respective ethylene glycol-protected analogues to the higher solubility of the PrG-protected monomer, oligomers, and polymer during polymerization.

The deprotection step is done in analogy to the literature (reflux in aqueous trifluoroacetic acid (TFA)) and produces PPTO with gravimetric yields of >100% due to the incompleteness of the deprotection (Figure 2a). The polymer likely starts precipitating as soon as the protecting groups are partially removed, inhibiting a full conversion. Qualitative evidence for a successful deprotection is given by the emergence of a strong vibrational band at 1678 cm^{-1} in the IR-spectrum of PPTO compared to that of $P(PTO_{PrPG})$ (Figure 2d), which signifies the presence of now unprotected carbonylic C═O double bond. This finding is also corroborated by ^{13}C CP-MAS NMR measurements (Figure S5). Thermal gravimetric analyses (TGA) show that the decomposition of protected $P(PTO_{PrG})$ proceeds at much lower temperatures compared to PPTO, giving further evidence for the absence of protecting groups in PPTO (Figure S6). In differential scanning calorimetry measurements, no significant thermal transitions are observed for either $P(PTO_{PrG})$ or PPTO (Figure S7).

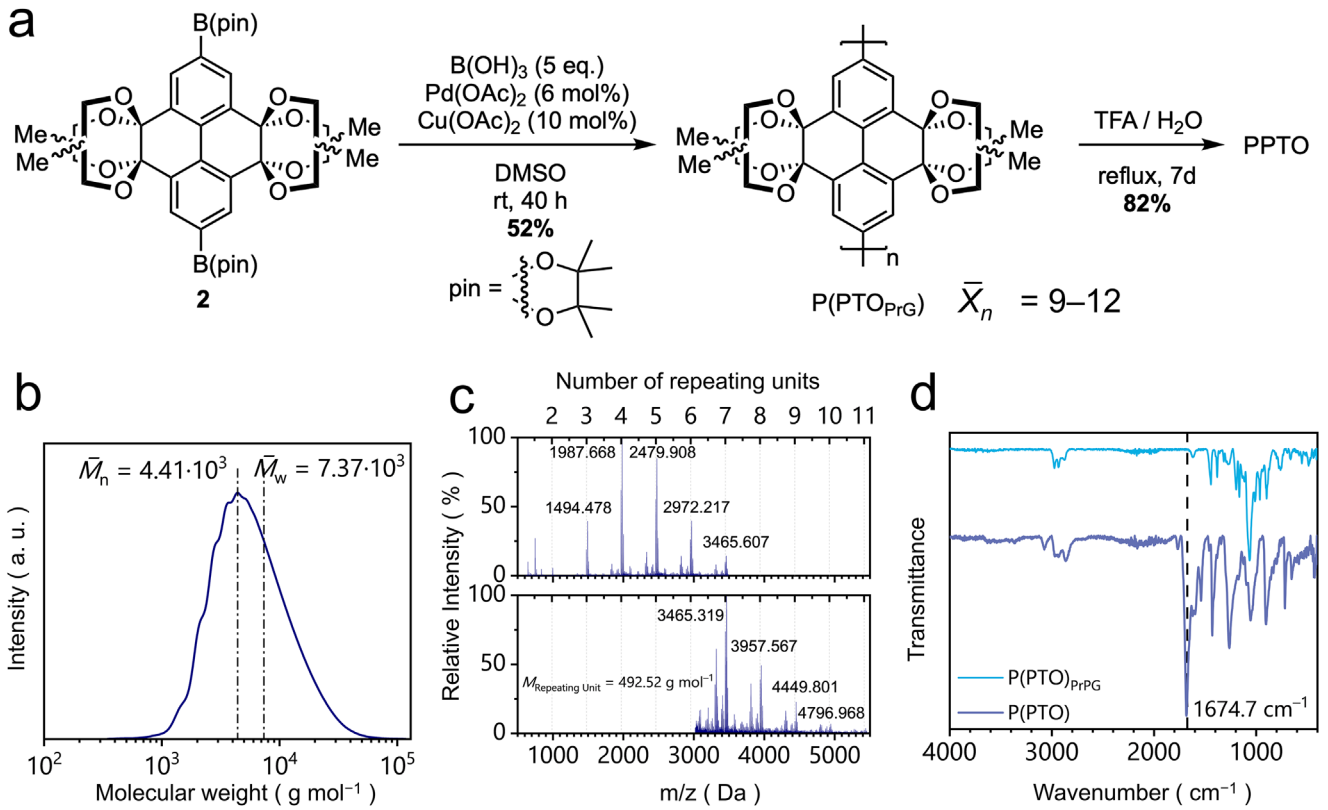

FIGURE 2 | (a) Improved synthetic pathway to PPTO from **2** using propylene glycol (PrG)-protection via oxidative homopolymerization to $P(PTO_{PrPG})$ followed by deprotection; (b) Molecular weight distribution of $P(PTO_{PrG})$ determined by gel-permeation chromatography (GPC) in THF (polystyrene standard, detector: UV 254 nm); (c) MALDI-MS spectra of $P(PTO_{PrG})$ covering the whole m/z range; (d) FTIR spectra of $P(PTO_{PrG})$ (top, blue) and PPTO (bottom, light blue) with carbonyl band at 1675 cm^{-1}.

Scanning electron microscopy (SEM) reveals a random bulk morphology of PPTO with a uniform distribution of the constituting elements C and O (Figures S8 and S9). The XRD pattern shows multiple peaks demonstrating a mixed-phase nature of PPTO (Figure S10a). The Raman spectrum (Figure S10b) displays the characteristic peaks at 1592 and 1689 cm^{-1}, corresponding to the C═C and C═O bond stretching vibrations [43]. This improved accessibility and characterization of the polymer provide a more reliable basis for the electrochemical analysis discussed below.

2.2 | Electrochemical Energy Storage Characterizations

The electrochemical performance of PPTO was investigated using 1 M $NaPF_6$ in diethylene glycol dimethyl ether (DEGDME), 1 M $NaClO_4$ in tetraethylene glycol dimethyl ether (TEGDME), and 4 M $NaPF_6$ in 1,2-dimethoxyethane (DME) as electrolytes and sodium foil as the negative electrode in coin-type half cells at room temperature. Out of these three electrolytes, the DEGDME-based electrolyte showed superior electrochemical performance (will be discussed later),. This electrolyte is able to form a uniform organic- and inorganic-based solid-electrolyte interphase (SEI) [52]. Further, PPTO is insoluble in this electrolyte (Figure S11). Due to their limited electrical conductivity, redox-active polymers as OAMs require the addition of a conductive carbon additive for electrode fabrication. CNTs have proven effective in this role due to their π-π-interations with the π-systems of OAMs, such as with PPTO, and high electrical conductivity [46, 53, 54]. CNTs have been demonstrated to have an ordered structure, high electrical conductivity, and a large surface area ($\geq$ 800 m^2 g^{-1}), favorable for efficient Na-ion diffusion [43, 55]. Polymers based on π-systems can wind around CNTs to provide a three-dimensional electronic conductive network for efficient electron transfer which leads to a high utilization of active sites [21, 46, 56]. To investigate the influence of CNTs vs. other conductive carbon additives, three different types of PPTO composites were investigated, as well as a free-standing electrode (binder-free). The PPTO@CNTs@KB composite electrode contains PPTO, CNTs, KB and poly(vinylidenedifluoride) (PVDF) binder in a 50:20:20:10 weight ratio (active material mass loading 0.5–0.6 mg cm^{-2}), whereas the PPTO with only KB (herein referred to as (PPTO@KB) and PPTO with only Super P (herein referred to as PPTO@Super P) composite electrodes contain PPTO, conductive carbon and PVDF binder in a weight ratio of 50:40:10 (active material mass loading 0.4–0.6 mg cm^{-2}). The free-standing binder-free PPTO electrode is a combination of PPTO and CNTs in a 1:2 weight ratio (active material mass loading 2.5–3.2 mg cm^{-2}). The electrochemical performance of these four types of composite electrodes in the 1 M $NaClO_4$ in TEGDME and 4 M $NaPF_6$ in DME electrolytes showed poor specific capacity and cycling stability as compared to the 1 M $NaPF_6$ in DEGDME electrolyte (Figures S12–S19). Thus, the DEGDME-based electrolyte was used in the following to evaluate the detailed electrochemical performance of the various PPTO composite electrodes.

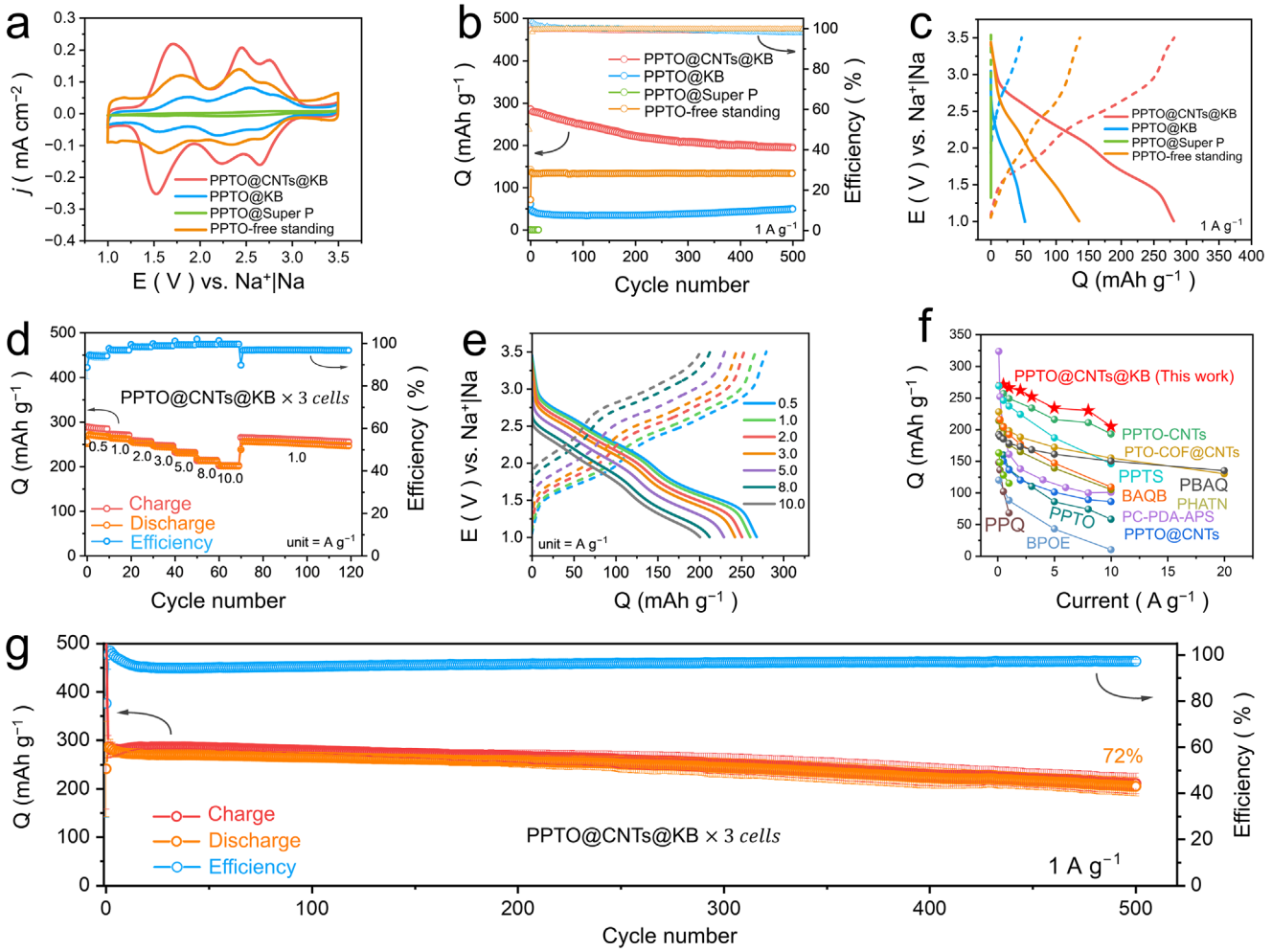

FIGURE 3 | Electrochemical characterization of PPTO electrodes vs. sodium with various conductive carbons in the 1 M $NaPF_6$ in DEGDME electrolyte at room temperature. (a) Cyclic voltammograms (CVs) at a scan rate of 0.3 mV s^{-1}. (b) Cycle life and corresponding (c) galvanostatic charge/discharge profiles of the second cycle. (d) Rate performance of PPTO@CNTs@KB electrodes as an average of three cells (with error bars). (e) Galvanostatic charge/discharge curves of the PPTO@CNTs@KB electrode at various current rates. (f) Comparison of the energy storage performance of PPTO@CNTs@KB electrodes in Na batteries with previous reports on PPTO and other electrode materials (references given in Table S3). (g) Long-term cycling performance of PPTO@CNTs@KB electrodes at 1.0 A g^{-1} as an average of three cells (with error bars).

The cyclic voltammograms (CVs) of the PPTO@CNTs@KB, PPTO@KB, PPTO@Super P, and PPTO free-standing electrodes at a scan rate of 0.3 mV s^{-1} in 1 M $NaPF_6$ DEGDME electrolyte are shown in Figure 3a. Except for the PPTO@Super P electrode (enlargement shown in Figure S20), all PPTO electrodes demonstrate similar peak shapes. The best-performing PPTO@CNTs@KB electrode exhibits three redox couples at potentials (anodic/cathodic peak potential) of 2.76/2.66 V, 2.45/2.24 V, and 1.71/1.52 V vs. Na^+/Na, respectively (Figure 3a and Figure S21). The half-wave potentials ($E_{1/2}$) for the three redox processes are 2.71, 2.35, and 1.62 V, respectively. This suggests several successive reduction steps of the carbonyl moieties in the PPTO framework. The lowest potential anodic peak (1.71 V) has a shoulder at ca. 1.87 V vs. Na^+/Na. While the appearance of these four peaks might indicate that all four one-electron redox reactions of the PTO units (see Figure 1) are addressable in the CV, DFT calculations suggest a different mechanism. According to DFT calculations, only two reduction steps for each PTO unit are possible within the CV potential range, while further peaks might be rationalized by dimer formation (see below). The PPTO@KB and PPTO free-standing electrodes (Figure 3a and Figures S22 and S23) show similar peaks, but with a shift in the redox potentials, along with lower peak-current densities and with decreased integral charge (based on the mass of the PPTO active material). The PPTO@CNTs@KB electrode delivers the highest peak-current density, suggesting the best utilization of the PPTO redox-active sites. This might be associated with efficient electron and ion transport within the electrode due to the addition of CNTs.

Galvanostatic cycling (Figure 3b) confirms that the PPTO@CNTs@KB electrode gives the best performance. While the PPTO@KB and PPTO free-standing electrodes deliver a discharge capacity of 52 and 136 mAh g^{-1} at 1.0 A g^{-1} (~2.4C, second cycle), corresponding to 11% and 33% of the theoretical specific capacity (412 mAh g^{-1}), respectively, the PPTO@CNTs@KB electrode delivers a maximum of 286 mAh g^{-1} (first cycle) discharge capacity with 72% retention over 500 cycles. In each case, the conductive carbon contributes to the specific capacity (CNTs-KB600 electrode: 65 mAh g^{-1}; KB600

electrode: 30 mAh g^{-1}; free-standing CNTs electrode: 46 mAh g^{-1}) as seen from purely carbon- and binder-based electrodes (Figures S24–S26). It is noted that the present electrode configuration employs a relatively low active-mass loading and a higher conductive carbon fraction to probe the intrinsic electrochemical behavior and mechanistic features of the PPTO material. The CNTs/Ketjen Black network plays a multifunctional role by providing electronic percolation, nanoscale confinement, and suppression of dissolution via π–π interactions. Thus, the CNTs/Ketjen Black framework not merely acts as a conductive additive, but as an integral structural component that governs charge transport and material stabilization. While capacitive contributions from the carbon matrix are present (see above), the dominant energy storage originates from the reversible carbonyl redox activity of PPTO.

While PPTO in its neutral form is insoluble in the used electrolyte (see above and Figure S11), in order to show a high cycling stability, the material also has to be insoluble in its reduced (discharged) form. We assume that the partial solubility of PPTO in its reduced state might be a reason for the lower capacity utilization in the PPTO@KB and PPTO@Super P compared to the PPTO@CNTs@KB electrodes. This is evidenced by a coloring of the separators after the first discharge and after 500 cycles (Figure S27) taken from PPTO@KB- and PPTO@Super P-based cells. In contrast, in the PPTO@CNTs@KB electrode, PPTO is efficiently immobilized, hindering its dissolution, as judged by the lack of separator coloring and, thus, resulting in a higher specific capacity and improved cycling stability. This finding is further supported by an experiment in which the various PPTO-electrodes were fully discharged and then soaked in the electrolyte (Figure S28). Over time, the PPTO@KB and PPTO@Super P electrodes show clear signs of dissolution/coloring of the electrolyte, whereas the PPTO@CNTs@KB electrode remains stable, exhibiting no dissolution in the electrolyte. Although the reduced dissolution is visually evident from electrolyte coloration, this conclusion is further supported by the significantly enhanced cycling stability and the 3D-conductive network revealed by tomography, which further collectively indicate effective immobilization of PPTO within the CNTs/Ketjen Black framework. Time-dependent density functional theory (TD-DFT) calculations of PTO and sodium-inserted PTO (PTO-4Na) further ascertain these findings (Figure S29). A significant redshift of the π—π^* absorption occurs after reduction. When sodium is inserted into the PTO unit during electrochemical reduction, the carbonyl groups (C═O) are reduced to conjugated enolates (C─O). This increases the size of the π-conjugated system, resulting in a smaller bandgap and redshifted absorption.

The galvanostatic charge/discharge profiles of the different PPTO-based electrodes within the 1.0 to 3.5 V voltage window are shown in Figure 3c. They clearly show the highest specific capacity being accessible for the PPTO@CNTs@KB electrode. The sloping charge/discharge profiles reflect the shape of the CV curves, showing successive reversible reduction of the carbonyl moieties of each PTO unit. The corresponding differential capacity plot is given in Figure S30. The average discharge potential (Figure S31) of the PPTO@CNTs@KB electrode is ~2.1 V vs. Na^+/Na, which is comparable to other carbonyl-based organic electrode materials [25, 46, 57–59].

The PPTO@CNTs@KB electrodes demonstrate a decent rate performance (Figure 3d,e) at different current rates (average of three cells given) with overall much higher accessible specific capacities as compared to the PPTO@KB- and PPTO-free-standing electrodes (Figure S32). Even at the high rate of 10 A g^{-1}, 201 mAh g^{-1} discharge capacity is accessible. The specific capacity is restored to the original value when the current is reduced back to 1.0 A g^{-1} after 70 cycles of varying current rates (Table S1). In cycle 71 at 1.0 A g^{-1}, the specific capacity reaches 256 mAh g^{-1}, corresponding to 97% of the initial capacity (264 mAh g^{-1}) in cycle 1. With this, the PPTO@CNTs@KB electrodes deliver an energy density of 549 Wh kg^{-1} (based on the mass of PPTO active material) at 0.05 A g^{-1} and even maintain 346 Wh kg^{-1} at 10.0 A g^{-1} (Figure S33). Furthermore, the electrodes deliver an energy density of 275 Wh kg^{-1} (based on the total mass of the electrode) at 0.05 A g^{-1} and maintain 173 Wh kg^{-1} at 10.0 A g^{-1} (Figures S34 and S35), comparable to or even better than previous reports on π-conjugated polymers [46, 58, 60–63]. A direct comparison with previously reported PTO-based and other related electrodes (in Na-based batteries) highlights the significant performance enhancement achieved in this work (Table S2). While earlier studies typically report moderate capacities and limited rate capability due to poor electronic conductivity and dissolution of active material, the PPTO@CNTs@KB electrode delivers a high reversible capacity of 286 mAh g^{-1} at 1 A g^{-1} and maintains 201 mAh g^{-1} even at 10 A g^{-1}. Furthermore, the extended cycling stability over 500 and 1000 cycles surpasses most prior reports. These results further establish PPTO@CNTs@KB electrode as one of the highest-performing PPTO-based cathodes reported to date, particularly under high-rate and long-term cycling conditions. The voltage plateaus are well preserved even at high current rates with low voltage polarization (Figure 3e). A significant voltage retention further underlines the good performance of the PPTO@CNTs@KB electrodes after keeping a fully charged cell (100% state of charge, SoC) at open-circuit voltage under no load for 10 h (Figure S36), which shows 76% voltage retention. This value can be assigned to the superior stability of the PPTO@CNTs@KB electrode and the less spontaneous side reaction of the electrolyte.

The specific discharge capacities at different current rates (1.0 to 10.0 A g^{-1}) we obtained with the PPTO@CNTs@KB electrodes using PPTO synthesized via the improved procedure are superior to previous reports on PTO or PPTO-based electrodes in Na batteries (Figure 3f and Table S3). In particular, they show a better electrochemical performance compared to PTO (small molecule)-based electrodes under the same electrochemical conditions in two different electrolytes (1 M $NaPF_6$ in DEGDME and 1 M $NaClO_4$ in TEGDME), which we investigated for comparison (Figures S37–S40). This demonstrates the crucial role of polymerization to mitigate the dissolution of active material into the electrolyte.

The PPTO@CNTs@KB electrodes demonstrate satisfactory long-term cycling stability at 1 A g^{-1}. An average of the data of three cells is shown in Figure 3g, highlighting the reproducibility of the measured data (for a separate plot, see Figure S41). The PPTO@CNTs@KB electrode delivers 205 mAh g^{-1} discharge capacity at the end of 500 charge/discharge cycles, which corresponds to 72% capacity retention with merely 0.05% capacity loss per cycle. The Coulombic efficiency remains at ~98%,

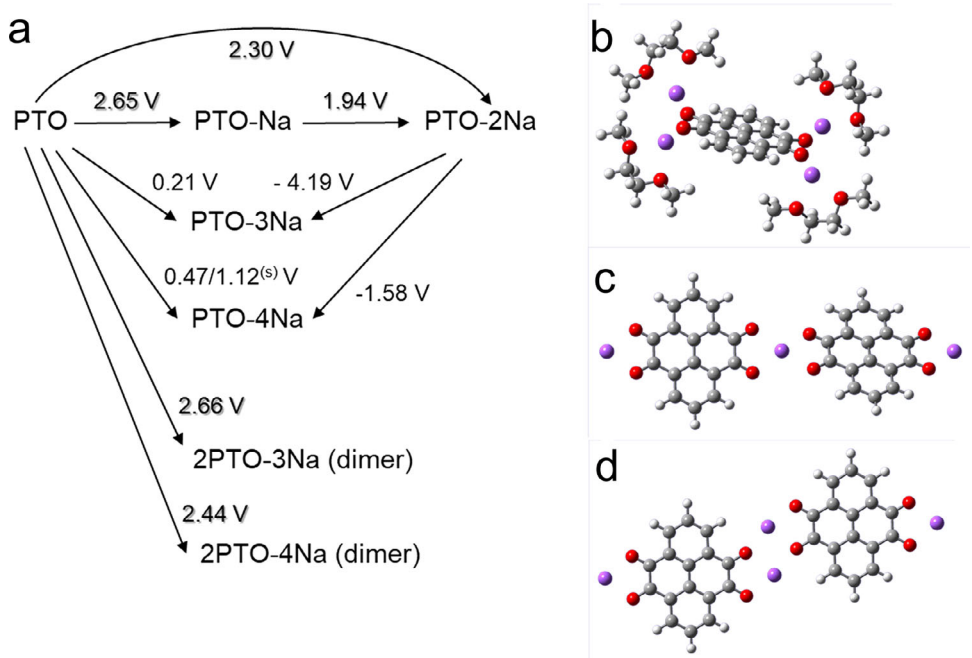

FIGURE 4 | (a) Diagram of calculated redox potentials (vs. Na^+/Na) of PTO in DEGDME (isodesmic model) and small PTO dimeric structures in DEGDME with Na^+ counter cations. (s) Explicit dimethoxyethane solvent molecules are included in the calculation (gas and solvent phase). Shadowed values are within the experimental CV voltage range. Geometry-optimized structures: (b) PTO-4Na with four explicit dimethoxyethane solvent molecules, (c) dimeric clusters of two PTO molecules and three Na atoms, and (d) of two PTO molecules and four Na atoms. Na atoms are colored violet, oxygen atoms red, carbon atoms gry, and hydrogen atoms white.

corresponding to stable cycling. To further evaluate the extended long-term cycling stability, the PPTO@CNTs@KB electrode was cycled up to 1000 cycles at 1 A g^{-1} current rate (Figure S42). The electrode retained 67% of its initial capacity, demonstrating durability and confirming the effectiveness of the conductive carbon network in stabilizing the active material over prolonged cycling. We assume that the superior long-term cycling stability of the PPTO@CNTs@KB electrode is primarily due to the strengthened interaction between the CNTs and the π-system of PPTO, which enhances reaction kinetics, improves Na-ion diffusion, and ensures the structural stability of the electrode. To demonstrate their utility, the coin cell assembled using the PPTO@CNTs@KB electrode vs. sodium-metal can power a red-light-emitting diode for ca. 60 min (Figures S43). Scaling up the PPTO content in the electrode, however, will require further electrode engineering. We investigated a PPTO@CNTs@KB electrode with 70 wt.% PPTO, which delivered lower specific capacities and poorer cycling stability, indicating the necessity of an adequate amount of carbon (CNTs + KB) in the final electrode composition (Figure S44).

2.3 | DFT Calculations on the Redox Reactions

To rationalize the experimentally observed redox peak potentials, DFT calculations were performed on PTO using two computational protocols: a direct reduction model and an isodesmic model, to theoretically predict the standard reduction potentials in solution (for details, see the Supporting Information). The electrode potential values obtained from both methods show good qualitative agreement. Figure 4a and Table S4 summarize the redox potentials calculated using the isodesmic model. The direct reductions of PTO to PTO-Na (one-electron process) and PTO-2Na (two-electron process) yield calculated redox potentials of 2.54 and 2.19 V, respectively. The first reduction differs by only 0.11 V from the experimental value of 2.65 V (Figure S37), indicating a very good correlation. All the calculated values for the different reduction processes are included in Table S4. The calculated potentials for the third and fourth PTO direct reductions to PTO-3Na and PTO-4Na, however, are out of the voltage range of the CV measurements (Figure 3). Calculations including four explicit solvent molecules (DME, for simplicity) close to the Na^+ in PTO-4Na (0.36 V potential) (Figure 4b) shift the cell potential by 0.65 V to a value of 1.01 V, which comes closer to the experimental values, but is still outside the CV range. On the other hand, the one-electron reduction of PTO-Na to PTO-2Na shows a potential of 1.83 V, which fits within the experimentally observed voltage range. In order to explain the further reduction peaks observed experimentally, small clusters formed by PTO-dimers with three or four Na-atoms were calculated (Figure 4c,d), and the corresponding potentials, 2.55 and 2.33 V, fit well within the voltage range (Figure 3).

In summary, DFT calculations predict that in the experimental voltage range, only two reduction steps of each PTO unit are possible, which would correspond to a theoretical specific capacity of 204.5 mAh g^{-1} for PPTO. According to the calculations, the presence of four peaks in the experimental CVs (see Figure 3a) of the PPTO-Na half cells could potentially be rationalized by the formation of PTO-dimers in their reduced form. Indeed, this theoretical prediction fits well with the experimental specific capacities—if the conductive carbon contribution is deducted—of the PPTO@CNTs@KB electrodes. Therefore, Na^+ insertion is proposed to proceed via a dimer-assisted mechanism, as suggested by DFT calculations and supported by experimental

observation. While direct spectroscopic identification of dimer intermediates remains challenging, the proposed mechanism is consistent with the observed reversible redox behavior and absence of phase transitions, suggesting a delocalized intermolecular interaction during Na^+ insertion.

2.4 | Ion-Insertion Properties

As the PPTO@CNTs@KB electrode exhibited a high rate capability, its kinetic properties were investigated by measuring CVs at different scan rates to differentiate between capacitive and faradaic contributions (Figure 5a) [64, 65]. The peak current (i) and the scan rate (ν) relation can be denoted as $i = a\nu^b$, where a and b are constant values. A b-value of 0.5 indicates a diffusion-controlled process, whereas the behavior is surface-controlled for b = 1 [66]. The fitted linear relationship between log(i) and log(ν) for the PPTO@CNTs@KB electrodes provides slopes in the range of 0.82–0.99, indicating a dominantly surface-controlled process (Figure S45). Furthermore, following Augustyn et al. [67], the capacitive ($k_1\nu$) and diffusion-controlled ($k_2\sqrt{\nu}$) contributions can be calculated according to the equation: $i = k_1\nu + k_2\sqrt{\nu}$. Accordingly, current values were recorded at successive points at an interval of 50 mV along the oxidation and reduction profiles of the CVs at various scan rates. With this, the calculated capacitive contribution amounts to 87% at a scan rate of 0.2 mV s^{-1} (Figure 5b) and increases to 95% at 1.0 mV s^{-1} (Figure 5c). These results evidence the superior redox kinetics of the PPTO@CNTs@KB electrode, where the rate of the electrochemical processes is not limited by the ion-diffusion rate to the redox sites.

Furthermore, the peak-to-peak voltage separation ($\Delta E = E_{p,a} - E_{p,c}$) is significantly smaller than in previous reports on PPTO across all the scan rates for the three redox processes (A1/C1, A2/C2, and A3/C3), indicating the superior reversibility of the redox (sodiation/desodiation) reactions (Figure 5d–g) [46, 57]. At the slowest scan rate (0.2 mV s^{-1}), the ΔE_p for the first redox process (A1/C1) is close to 118 mV and only reaches 164 mV at a higher scan rate (1.0 mV s^{-1}) (Figure 5g). Similar behavior is observed for the second (A2/C2) and third (A3/C3) redox processes.

Subsequently, the Na^+ diffusion coefficients (D_{Na+}) were evaluated using the galvanostatic intermittent titration technique (GITT) (Figure S46, more details in the accompanying text in the Supporting Information). D_{Na+} is high (10^{-10} cm^2 s^{-1}) until a voltage of ca. 3.1 V is reached, after which the D_{Na+} value decreases (10^{-12} cm^2 s^{-1}), suggesting a relatively sluggish process mainly owing to the phase transition (Figure 5h) [68]. However, D_{Na+} stays relatively high (10^{-10} cm^2 s^{-1}) throughout the discharge process, which is an improvement over previous reports (Table S5). This confirms that the PPTO@CNTs@KB electrode enables fast Na^+ transfer kinetics and efficient ion diffusion. Notably, the slight difference obtained between the charge and discharge capacities in the GITT profile originates primarily from kinetic and interfacial asymmetries during Na^+ insertion and extraction. Although the carbonyl redox reaction in PPTO is thermodynamically reversible, Na^+ transport is accompanied by polarization arising from Na^+ desolvation in the ether-based electrolyte, charge-transfer resistance at the electrode–electrolyte interface, and solid-state diffusion within the polymeric framework. These effects shift the operating voltage during current pulses and can lead to premature attainment of the cutoff voltage in one direction, resulting in an apparent capacity mismatch. In addition, minor irreversible Na^+ consumption associated with the interfacial side reactions and incomplete relaxation during GITT rest periods further contributes to the asymmetry.

Electrochemical impedance spectroscopy (EIS) was performed to further evaluate the reaction kinetics (Figure S47). The EIS measurement at open-circuit voltage (OCV) after one activation cycle reveals a significant decrease in the charge-transfer resistance (R_{ct}, the arc in the high-frequency zone). The R_{ct} value decreased to ~96 from ~830 Ω after the activation process (Figure S47a), which is associated with electrode wetting and ion transport within the polymer matrix and also due to the formation of a facile solid-electrolyte interface (SEI). Thus, the charge-transfer resistance over the electrode surface improves, thereby lowering the impedance [57, 69]. Furthermore, the EIS measurements at various discharge/charge states reveal a significant reduction in the R_{ct} value (Figure S47c). The decreasing trend during the discharge process might be due to the improved contact between the composite electrode and the electrolyte, and the formation of a stable SEI layer, subsequently leading to better ion and charge transport. During the charging process, R_{ct} slightly increases, in agreement with the GITT results. However, beyond 2.65 V, the charge transfer resistance again decreases until the charge process completes at 3.5 V.

2.5 | Investigation of Charged/Discharged Electrodes

The Na^+ insertion mechanism in the PPTO@CNTs@KB electrode was evaluated by various ex situ characterization techniques at different states of charge and discharge (Figure 6a). As shown in Figure 6b, the high-resolution XPS C 1s spectrum can be deconvoluted into five peaks, corresponding to C—C/C—H, C—O (with PVDF CH_2), C═O, O—C═O, and C—F groups. The carbonyl peak originates from the pristine PPTO composite cathode, while other peaks are mainly associated with conductive carbon and binder components [21]. Upon the first discharge, the intensity of the C═O peak significantly decreases, whereas the relative intensity of the C—O peak increases, indicating the reduction of C═O to C—O bonds in the discharged state of the PPTO. During the subsequent first charge, upon oxidation, C—O bonds are converted back to C═O bonds, as evidenced by the decreased intensity of the C—O peak and a relative increase in the C═O peak intensity.

This trend is similarly observed in the second discharge and charge cycle. The O 1s spectra display a parallel behavior, characterized by a decrease in the intensity of the C═O peak, owing to aromatization, and a corresponding increase in the C—O peak in the discharged state (Figure 6c). Upon full charging, the intensities of these two peaks are restored, reflecting the highly reversible redox activity of the C═O groups in PPTO. In addition, a sodium Auger (KLL) peak is observed in the O 1s spectra of the cycled electrodes, which is consistent with the literature [21, 70]. Furthermore, in the XPS survey spectra, the relative intensity of the Na 1s peak becomes prominent during

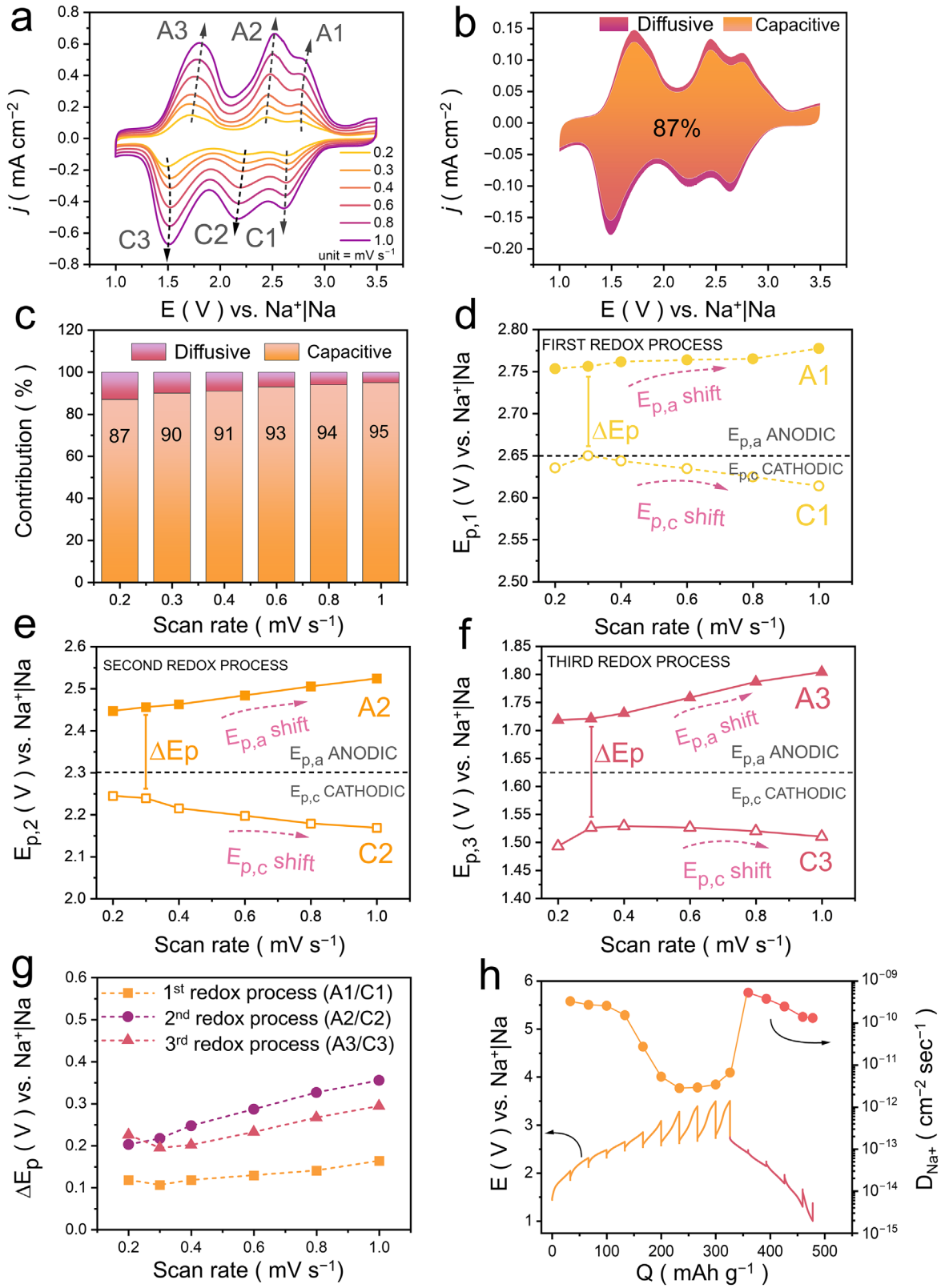

FIGURE 5 | Electrochemical kinetics evaluation of the PPTO@CNTs@KB electrodes. (a) CV curves at various scan rates. The labels A1/A2/A3 and C1/C2/C3 refer to the anodic and cathodic peak potentials, respectively. (b) The fitted CV curve at 0.2 mV s^{-1} with capacitive contribution. (c) Charge contribution at various scan rates. (d–f) Peak-potential position at various can rates for the first (A1/C1), second (A2/C2), and third (A3/C3) redox processes, respectively. (g) Peak potential difference as a function of scan rate for the first redox process (A1/C1/ΔE), second redox process (A2/C2/ΔE), and third redox process (A3/C3/ΔE), respectively. (h) GITT curve at a current rate of 200 mA/g and corresponding sodium-ion diffusion coefficient. (Orange color indicates charge process, and reddish color discharge).

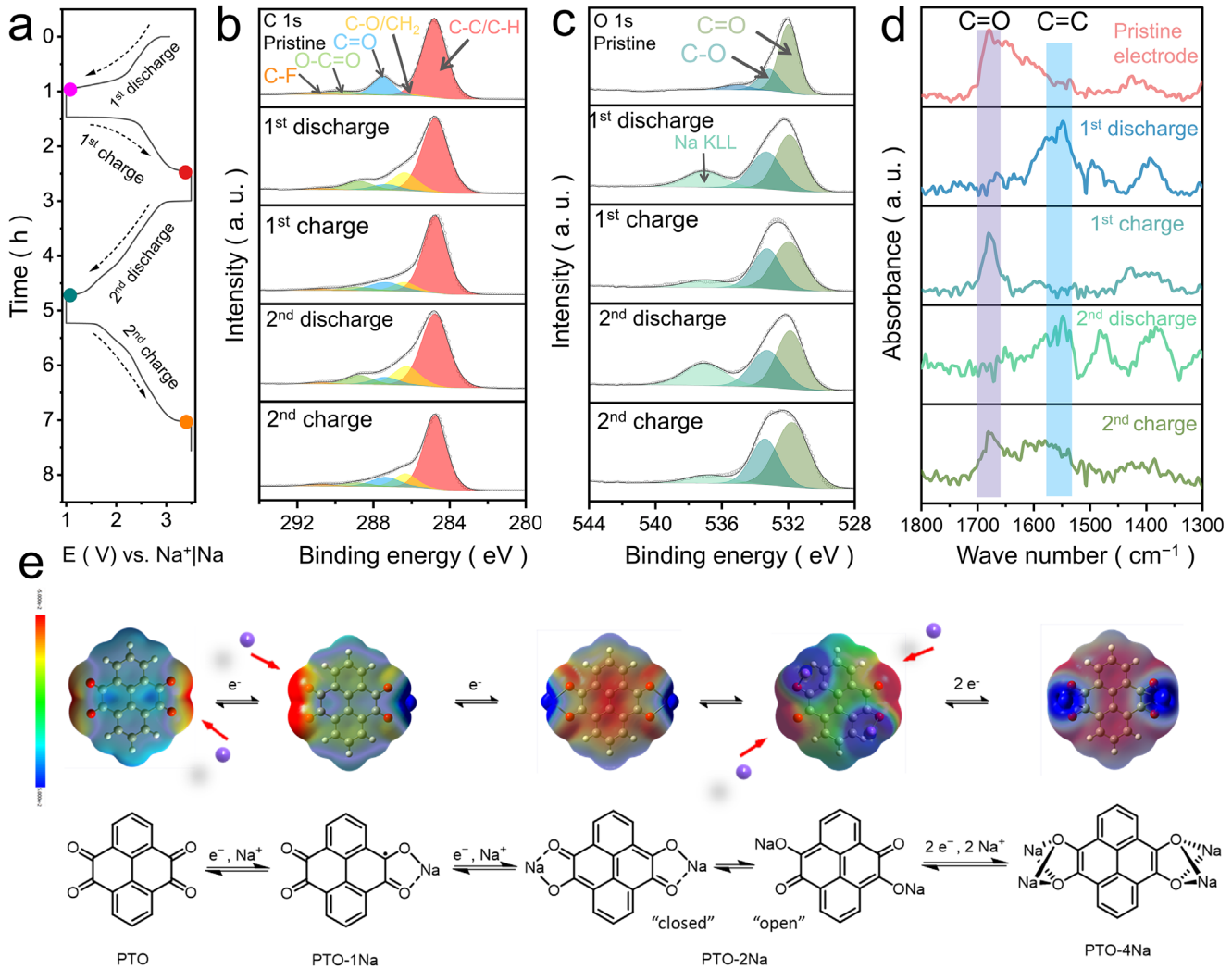

FIGURE 6 | (a) Charge/discharge profiles of the PPTO@CNTs@KB electrode at various states in the first two cycles, with 30 min hold at the end voltage in the corresponding cycles. (b) Ex situ C 1s; and (c) O 1s XPS measurements at different charged/discharged states. (d) Ex situ ATR-FTIR spectra at different charged/discharged states. (e) Molecular electrostatic potential (MEP) surfaces in the gas phase (top line) of PTO, PTO-1Na, PTO-2Na, and PTO-4Na (bottom line, chemical formula). Na^+ is represented by violet balls, and red arrows point to the most probable electrophilic Na^+ binding site. Thermal scale: Red to blue, respectively, negative to positive values.

the discharge process and subsequently weakens at the end of the charge process, indicating the reversible insertion of Na^+ (Figure S48). This is further evidenced by an SEM-EDS analysis, which shows a higher Na content in the discharged compared to the charged state (Figures S49 and S50) and a uniform distribution of the constituting elements over the electrode surface (Figures S51–S55). Additionally, the morphology of the composite electrode remains unchanged, not only after initial charge/discharge cycles, but also after long-term cycling (Figure S56). This post-cycling SEM analysis (Figure S56f) confirms that the PPTO@CNTs@KB electrode maintains its structural integrity after 500 cycles, indicating that the observed capacity fading is not associated with severe morphological degradation. Ex situ ATR-FTIR spectroscopy provides further evidence for the reversible change in the C═O group during the charge/discharge process (Figure 6d and Figure S57). The peak assigned to the C═O groups disappears during discharge with an increase in the peak intensity of the C═C bond, confirming the reduction of the C═O group [43, 57]. Encouragingly, the C═O peak regains intensity upon charging until recovering its pristine state. DFT calculations shed light on structural changes within the PTO units upon reduction (Figure S58). Upon successive reduction of the PTO unit with Na^+, the C—O bond length increases from 1.21 (characteristic of a double bond) to 1.28 Å for the two-fold reduction and even further to 1.35 Å (stronger single bond character) in the case of the four-fold reduction. Concomitantly, the C—C bond distance between the carbonyl groups decreases from 1.54 to 1.48 and 1.40 Å (PTO-2Na and PTO-4Na, respectively), reflecting enhanced aromaticity. Moreover, the experimental bond distance analysis reveals variations of less than 3% during PTO reductions. In addition, the DFT calculations reveal that the Na-ions preferentially coordinate with both oxygen atoms of the PTO unit in the optimised geometry conformation, consistent with the previous report [46]. Similarly, the ex situ Raman spectra display variations and provide evidence of the redox mechanism of the PPTO@CNTs@KB electrode during the charge/discharge process (Figure S60). At the pristine state (Figure S60a), the PPTO electrode exhibits the characteristic stretching modes corresponding to the C═O (1690 cm^{-1}) and the

C═C (1535 cm^{-1}) bonds of the PTO framework. The peaks at 1350 and 1590 cm^{-1} are characteristic of the D and G-band of the conductive carbon additives (CNTs + Ketjen Black). Upon discharge, a slight downshift (1535 ⟶ 1529 cm^{-1}) in the C═C stretching mode is observed, suggesting an increase in aromaticity of the C═C bond within the pyrene ring framework (Figure S60b) [43]. Additionally, the C═O stretching mode undergoes splitting, resulting in the appearance of a new band at a lower wavenumber (1673 cm^{-1}), which is attributed to the formation of a sodium enolate bond (Na—O—C) [43]. The redshift of the carbonyl vibration by ~17 cm^{-1} (1690 ⟶ 1673 cm^{-1}) is indicative of weakened C═O bonds due to electron delocalization and Na^+ interaction, confirming a reversible enolization process upon sodiation. During the subsequent charging (Figure S60c), the peak position and intensities of the C═C and C═O bonds return nearly back to their pristine state, evidencing restoration of the π-conjugated framework and reformation of carbonyl groups, correlating with the removal of the Na^+. This indicates that the redox reaction involving the C═O group in the pyrene ring network is highly reversible. Meanwhile, the D (1350 cm^{-1}) and G (1590 cm^{-1}) bands associated with the CNTs and Ketjen Black matrix remain largely unchanged throughout cycling, suggesting good structural stability of the conductive network. Thus, the various ex situ characterizations methods demonstrate that the carbonyl group of the PPTO framework is responsible for facilitating the reversible storage of the Na^+ during the charge–discharge process involving the redox reaction, as represented in Figure 1.

To further investigate the sodium-ion-insertion mechanism, molecular orbital energies were calculated, specifically the lowest unoccupied molecular orbital/highest occupied molecular orbital (LUMO/HOMO) energy level of PTO and the reduced PTO-nNa (n = 1–4) species (Figure S59), along with the molecular electrostatic potential (MEP) maps (Figure 6e). In PTO-1Na, the LUMO is localized on the dione site opposite the first reduction site, which is also found for PTO-3Na. The HOMO of the reduced PTO-2Na exhibits electron density delocalization through the center of the PTO, whereas in the case of PTO-3Na and PTO-4Na, delocalization occurs through the periphery of the pyrene backbone. PTO-1Na shows a mixed behavior. Interestingly, the bandgap strongly reduces from the pristine PTO (3.50 eV) to the two-times reduced form, PTO-2Na (0.77 eV), and then successively increases again for PTO-4Na (1.92 eV/2.85 eV) in both the gas and the solvated phase (Figure S61).

As mentioned before, the Na^+ preferentially accept a coordinative bond from both neighbouring oxygen atoms in the reduced PTO species. Even in the case of a four-fold reduction, the Na^+ favorably form a small cluster with equal bond distances to both neighbouring oxygen atoms (2.25 Å) and Na—Na bond distances of 3.17 Å, below the value of 3.71 Å for metallic sodium. We describe this conformation as "closed". Both the "closed" and the "open" conformation can be visualized for PTO-2Na in Figure 6e (bottom): in the "open" conformation, which is metastable, the Na^+ are bound by only one oxygen. The "closed" form in solution is 1.75 to 2.43 eV (40 to 56 kcal/mol) more stable than the "open" one.

In the MEP surfaces (Figure 6e), the red-colored positions account for a higher negative charge distribution, making coordination of Na^+ more likely, which are the oxygen atoms in pristine PTO and PTO-1Na. In PTO-2Na ("closed" form), the negative charge is distributed not only at the oxygen atoms but also in the PTO core. In the "open" conformation, on the contrary, the negative charge is localized at the not-bound oxygen atoms, and therefore this conformer should be more relevant for successive coordination of Na^+, for example, to PTO-4Na, as depicted in Figure 6e. Nevertheless, we recall at this point the fact that the calculations show the "open" conformer to be about 2.43 eV less stable than the "closed" one in solution.

2.6 | Electrode Tomography

The 3D microstructures of the PPTO@SuperP and PPTO@CNTs@KB electrodes were investigated via focused-ion-beam scanning-electron microscopy (FIB-SEM). Further details regarding tomographic imaging, the segmentation into active material (AM), carbon-binder domain (CBD, i.e., the union of conductive additives and binder), and pore space, as well as the considered geometrical descriptors, can be found in the Supporting Information. Figure 7 shows 3D renderings of cubic cutouts of the segmented tomographic image data of PPTO@SuperP (top) and PPTO@CNTs@KB (bottom).

The results of the statistical image analysis are shown in Figure 8. Figure 8a shows that the PPTO@CNTs@KB electrode has a higher AM volume fraction compared to the PPTO@SuperP electrode, offering a larger theoretical capacity. This also holds true for the CBD, which in turn results in a lower porosity of the PPTO@CNTs@KB electrode compared to the PPTO@SuperP electrode. As can be seen in Figure 8b, there is a significant difference in the shape of the distribution of local volume fraction for the CBD. More precisely, the broader distribution in the case of the PPTO@CNTs@KB electrode indicates a more pronounced heterogeneity of the electrode structure compared to PPTO@SuperP. Figure 8c shows that despite the difference in volume fraction of the active material phase, the specific surface area is nearly identical. With regard to the CBD and the pore space, the PPTO@CNTs@KB electrode exhibits a larger specific surface area compared to the SuperP-based electrode. This is particularly interesting in the case of the pore space, since the PPTO@CNTs@KB electrode has a lower porosity, which indicates a significantly finer pore space. Figure 8d shows the mean chord length of the three phases in *x*-, *y*-, and *z*-direction. With respect to the CBD and the pore space, there are no pronounced anisotropy effects. However, the mean chord length of the active material phase is significantly lower in the *y*-direction than in *x*- and *z*-direction for the PPTO@CNTs@KB electrode. Moreover, this electrode exhibits a significantly larger mean chord length of the active material compared to the PPTO@SuperP electrode, which indicates larger active material clusters, which, in combination with a larger volume fraction of active material, seems to be beneficial with respect to the electrochemical performance. Figure 8e shows the mean geodesic tortuosity of the three phases, where a similar behavior as in the case of the mean chord length can be observed. More precisely, the *y*-direction plays a particular role since it is the only direction that differs compared to the *x*- and *z*-directions when considering the active material or the pore space. Finally, we observe that the pore space and the CBD are completely

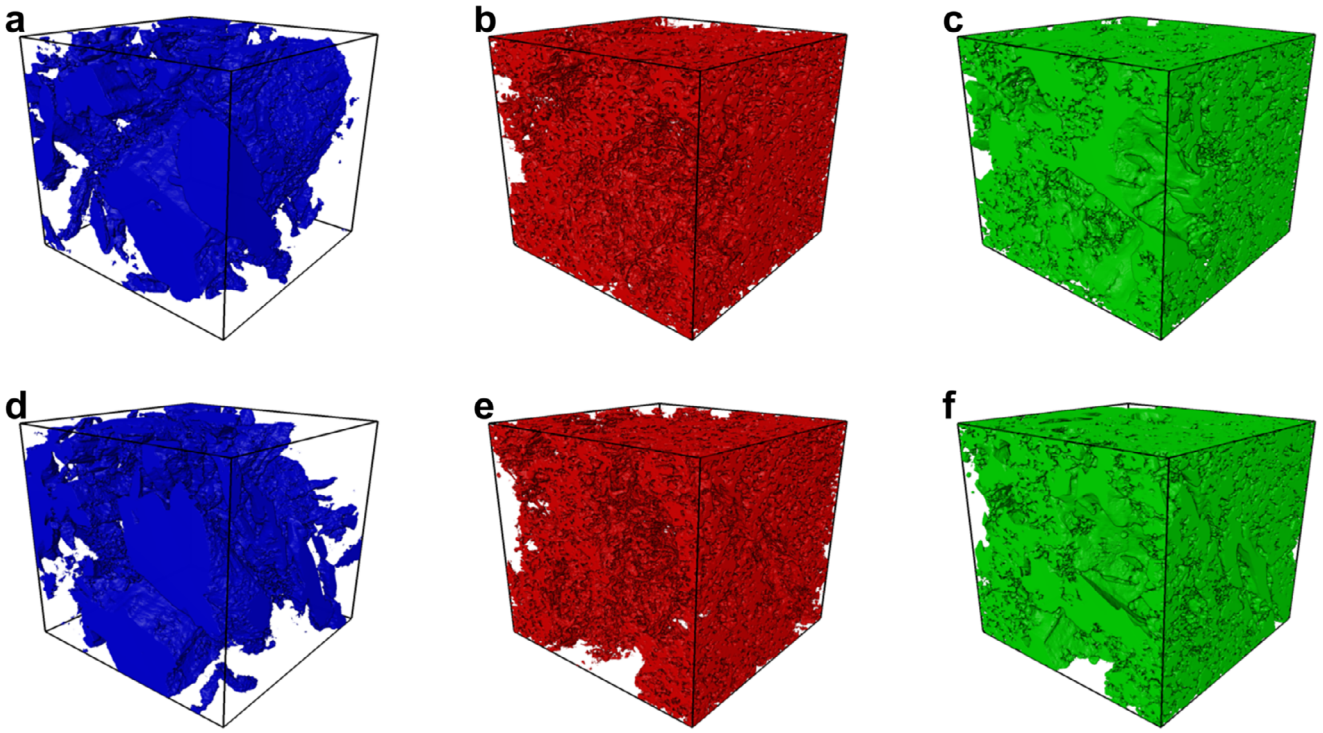

FIGURE 7 | 3D renderings of a cubic cutout (7 μm × 7 μm × 7 μm) of PPTO@SuperP (top) and PPTO@CNTs@KB (bottom), where active material, carbon-binder domain (CBD), and pore space are shown in blue (a, d), red (b, e), and green (c, f), respectively.

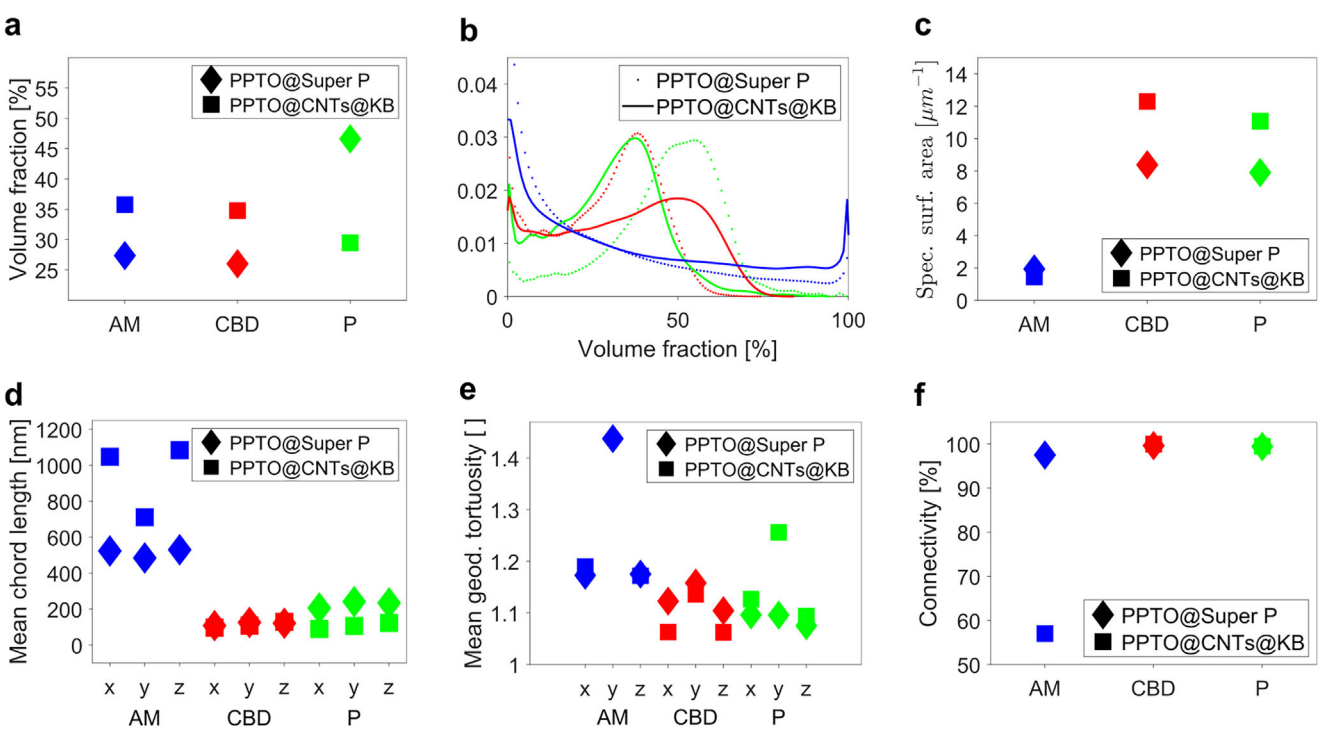

FIGURE 8 | (a) Volume fraction, (b) distribution of local volume fraction, (c) specific surface area, (d) mean chord length, (e) mean geodesic tortuosity, and (f) connectivity for the PPTO@SuperP and PPTO@CNTs@KB electrode based on the segmented 3D FIB-SEM data. Note that active material, CBD, and pore space are shown in blue, red, and green, respectively. Note that the mean chord length and mean geodesic tortuosity are computed in *x*-, *y*-, and *z*-direction.

connected, see Figure 8f. Note that the largest connected active material region of the PPTO@CNTs@KB electrode accounts for 57% of the volume of the active material phase, and the second largest connected component accounts for 35.2%. Furthermore, the disconnected active material phase in the case of PPTO@CNTs@KB is unlikely to worsen the electrochemical performance due to the completely connected CBD that ensures proper electric transport.

3 | Conclusions

In summary, we developed a nickel-free and scalable synthesis of poly(pyrene-4,5,9,10-tetraone) (PPTO) via Pd/Cu-catalyzed oxidative homopolymerization of propylene glycol-protected PTO boronic esters, overcoming the limitations of the conventional Ni-mediated YAMAMOTO coupling in terms of yield, solubility, and environmental impact. By optimizing the conductive carbon networks, we systematically demonstrate that PPTO@CNTs@Ketjen Black composite electrodes exhibit favorable performance in Na-based half cells, delivering a reversible capacity of 286 mAh g^{-1} at 1 A g^{-1}, and an acceptable long-term cycling stability (72% and 67% retention over 500 and 1000 cycles, respectively), and achieve a rate capability of 201 mAh g^{-1} at 10 A g^{-1}. Ex situ spectroscopic analyses and quantum-chemical calculations reveal a reversible two-electron carbonyl redox mechanism with contributions from intermolecular interactions and stabilized by extended π-conjugation, while kinetic investigations highlight rapid Na^+ diffusion and predominantly capacitive charge storage. Structural analysis further reveals that the percolated conductive network plays a critical role in maintaining electronic connectivity, confining the active material, and mitigating dissolution through nanoscale confinement. Furthermore, 3D-tomographic imaging underscores the critical role of the CNTs/Ketjen Black network in immobilizing PPTO and stabilizing the electrode microstructure. Collectively, this work demonstrates how rational synthetic design, coupled with electrode architecture engineering, can unlock the full potential of carbonyl polymers as a high-performance organic cathode for next-generation sodium-based batteries. Future efforts could focus on increasing areal mass loading and reducing conductive additive content to further evaluate practical applicability.

Author Contributions

M.A. and B.E. designed the battery concept of this project. R.W. and B.E. designed the synthesis concept. M.A. prepared the PPTO composite electrode and all other electrodes in this report. All the cell fabrication, electrochemical testing, kinetic measurements, impedance test, analysis, etc., and pre- and post-cycling characterizations, data evaluation, and analyses were performed by M.A. Physical characterizations of PPTO, viz., XRD, FT-IR, Raman, FEG-SEM, and EDS, were conducted by M.A., R.W., and N.K. R.W. synthesized and characterized PPTO and its precursors. N.K. conducted PPTO up-scaling experiments. E.M.-O. performed the DFT calculations. M.O. and I.M. conducted and interpreted the FIB-SEM experiments. B.P. and V.S. performed statistical image analysis of the resulting 3D image data. T.D. acquired and evaluated the XPS data. B.E. supervised and directed the research. M.A. wrote the manuscript in close exchange with B.E. and with input from all authors. All authors discussed and revised the manuscript and gave approval to its final version.

Acknowledgements

This research was funded by the Deutsche Forschungsgemeinschaft (DFG, German Research Foundation) under Project IDs 390874152 (POLiS Cluster of Excellence, EXC 2154), 441215516, 441236036, and 422726248 (all three SPP 2248 Polymer-based batteries), 445470598, 445471097, 445471845, 528773185, and INST 40/575-1 FUGG (JUSTUS 2 cluster). This work contributes to the research performed at CELEST (Center for Electrochemical Energy Storage Ulm-Karlsruhe). The authors acknowledge support by the state of Baden-Württemberg through bwHPC.

Open access funding enabled and organized by Projekt DEAL.

Conflicts of Interest

The authors declare no conflicts of interest.

Data Availability Statement

The data that support the findings of this study are openly available in Zenodo at https://doi.org/10.5281/zenodo.18443422, reference number 18443422.

References

1. Y. Tian, G. Zeng, A. Rutt, et al., "Promises and Challenges of Next-Generation "Beyond Li-ion" Batteries for Electric Vehicles and Grid Decarbonization," *Chemical Reviews* 121 (2021): 1623–1669, https://doi.org/10.1021/acs.chemrev.0c00767.

2. R. Usiskin, Y. Lu, J. Popovic, et al., "Fundamentals, Status And Promise Of Sodium-Based Batteries," *Nature Reviews Materials* 6 (2021): 1020–1035, https://doi.org/10.1038/s41578-021-00324-w.

3. Y. Jayamkondan, T. R. Penki, and P. K. Nayak, "Recent Advances And Challenges In The Development Of Advanced Positive Electrode Materials For Sustainable Na-Ion Batteries," *Materials Today Energy* 36 (2023): 101360, https://doi.org/10.1016/j.mtener.2023.101360.

4. I. Hasa, S. Mariyappan, D. Saurel, et al., "Challenges Of Today For Na-Based Batteries Of The Future: From Materials To Cell Metrics," *Journal of Power Sources* 482 (2021): 228872, https://doi.org/10.1016/j.jpowsour.2020.228872.

5. J. Hu, Y. Hong, M. Guo, et al., "Emerging Organic Electrodes For Na-Ion And K-Ion Batteries," *Energy Storage Materials* 56 (2023): 267–299, https://doi.org/10.1016/j.ensm.2023.01.021.

6. S. Lee, J. Hong, and K. Kang, "Redox-Active Organic Compounds for Future Sustainable Energy Storage System," *Advanced Energy Materials* 10 (2020): 2001445, https://doi.org/10.1002/aenm.202001445.

7. H. Zhang, Y. Gao, X. H. Liu, et al., "Organic Cathode Materials for Sodium-Ion Batteries: From Fundamental Research to Potential Commercial Application," *Advanced Functional Materials* 32 (2022): 2107718, https://doi.org/10.1002/adfm.202107718.

8. B. Häupler, A. Wild, and U. S. Schubert, "Carbonyls: Powerful Organic Materials for Secondary Batteries," *Advanced Energy Materials* 5 (2015): 1402034, https://doi.org/10.1002/aenm.201402034.

9. Y. Wu, R. Zeng, J. Nan, D. Shu, Y. Qiu, and S. Chou, "Quinone Electrode Materials for Rechargeable Lithium/Sodium Ion Batteries," *Advanced Energy Materials* 7 (2017): 1700278, https://doi.org/10.1002/aenm.201700278.

10. A. Jouhara, L. Rzesny, V. Rialland, C. Latouche, P. Poizot, and B. Esser, "Fusing Thiadiazole and Terephthalate: A Concept to Promote the Electrochemical Performance of Conjugated Dicarboxylates," *ChemSusChem* 16 (2023): 202300286, https://doi.org/10.1002/cssc.202300286.

11. M. E. Speer, C. Sterzenbach, and B. Esser, "Evaluation of Cyclooctatetraene-Based Aliphatic Polymers as Battery Materials: Synthesis, Electrochemical, and Thermal Characterization Supported by DFT Calculations," *ChemPlusChem* 82 (2017): 1274–1281, https://doi.org/10.1002/cplu.201700356.

12. G. Desmaizieres, M. E. Speer, I. Thiede, et al., "Dibenzo[a,e]Cyclooctatetraene-Functionalized Polymers as Potential Battery Electrode Materials," *Macromolecular Rapid Communications* 42 (2021): 2000725, https://doi.org/10.1002/marc.202000725.

13. P. Acker, M. E. Speer, J. S. Wössner, and B. Esser, "Azine-Based Polymers With A Two-Electron Redox Process As Cathode Materials For Organic Batteries," *Journal of Materials Chemistry A* 8 (2020): 11195–11201, https://doi.org/10.1039/D0TA04083E.

14. G. Dai, T. Wu, H. Chen, and Y. Zhao, "Quaternary Nitrogen Redox Centers For Battery Materials," *Current Opinion in Electrochemistry* 29 (2021): 100745, https://doi.org/10.1016/j.coelec.2021.100745.

15. H. Dong, N. Kang, L. Li, L. Li, Y. Yu, and S. Chou, "Versatile Nitrogen-Centered Organic Redox-Active Materials for Alkali Metal-Ion Batteries," *Advanced Materials* 36 (2024): 2311401, https://doi.org/10.1002/adma.202311401.

16. G. Studer, A. Schmidt, J. Büttner, et al., "On A High-Capacity Aluminium Battery With A Two-Electron Phenothiazine Redox Polymer As A Positive Electrode," *Energy & Environmental Science* 16 (2023): 3760–3769, https://doi.org/10.1039/D3EE00235G.

17. P. Acker, J. S. Wössner, G. Desmaizieres, and B. Esser, "Conjugated Copolymer Design In Phenothiazine-Based Battery Materials Enables High Mass Loading Electrodes," *ACS Sustainable Chemistry & Engineering* 10 (2022): 3236.

18. F. Otteny, V. Perner, C. Einholz, et al., "Bridging the Gap Between Small Molecular π-Interactions and Their Effect on Phenothiazine-Based Redox Polymers in Organic Batteries," *ACS Applied Energy Materials* 4 (2021): 7622–7631, https://doi.org/10.1021/acsaem.1c00917.

19. J. C. Barbosa, A. Fidalgo-Marijuan, J. C. Dias, et al., "Molecular Design Of Functional Polymers For Organic Radical Batteries," *Energy Storage Materials* 60 (2023): 102841, https://doi.org/10.1016/j.ensm.2023.102841.

20. H. Yang, J. Lee, J. Y. Cheong, et al., "Molecular Engineering Of Carbonyl Organic Electrodes For Rechargeable Metal-Ion Batteries: Fundamentals, Recent Advances, And Challenges," *Energy & Environmental Science* 14 (2021): 4228–4267, https://doi.org/10.1039/D1EE00419K.

21. M. Adil, M. Schmidt, J. Vogt, T. Diemant, M. Oschatz, and B. Esser, "Mitigating Dissolution to Enhance the Performance of Pillar [5] quinone in Sodium Batteries," *Batteries & Supercaps* 7 (2024): 202400312.

22. Y. Liang, P. Zhang, and J. Chen, "Function-Oriented Design Of Conjugated Carbonyl Compound Electrodes For High Energy Lithium Batteries," *Chemical Science* 4 (2013): 1330, https://doi.org/10.1039/c3sc22093a.

23. H. Cui, P. Hu, Y. Zhang, W. Huang, and A. Li, "Research Progress of High-Performance Organic Material Pyrene-4,5,9,10-Tetraone in Secondary Batteries," *ChemElectroChem* 8 (2021): 352–359, https://doi.org/10.1002/celc.202001396.

24. W. Deng, W. Shi, S. Wang, et al., "A Polypropylene (PP) Supported Solid Polymer Electrolyte Enables High-Stability Organic Lithium Batteries At Low Temperature," *Physical Chemistry Chemical Physics* 24 (2022): 14424–14429, https://doi.org/10.1039/D1CP05678F.

25. F. Hao, X. Chi, Y. Liang, et al., "Taming Active Material-Solid Electrolyte Interfaces With Organic Cathode for All-Solid-State Batteries," *Joule* 3 (2019): 1349–1359, https://doi.org/10.1016/j.joule.2019.03.017.

26. X. Chi, F. Hao, J. Zhang, et al., "A High-Energy Quinone-Based All-Solid-State Sodium Metal Battery," *Nano Energy* 62 (2019): 718–724, https://doi.org/10.1016/j.nanoen.2019.06.005.

27. W. Xiong, W. Huang, M. Zhang, P. Hu, H. Cui, and Q. Zhang, "Pillar[5]quinone–Carbon Nanocomposites as High-Capacity Cathodes for Sodium-Ion Batteries," *Chemistry of Materials* 31 (2019): 8069–8075, https://doi.org/10.1021/acs.chemmater.9b02601.

28. A. Jaffe, A. Saldivar Valdes, and H. I. Karunadasa, "Quinone-Functionalized Carbon Black Cathodes for Lithium Batteries With High Power Densities," *Chemistry of Materials* 27 (2015): 3568–3571, https://doi.org/10.1021/acs.chemmater.5b00990.

29. B. Esser, "Redox Polymers as Electrode-Active Materials for Batteries," *Organic Materials* 1 (2019): 63–70.

30. T. Nokami, T. Matsuo, Y. Inatomi, et al., "Polymer-Bound Pyrene-4,5,9,10-tetraone for Fast-Charge and -Discharge Lithium-Ion Batteries With High Capacity," *Journal of the American Chemical Society* 134 (2012): 19694–19700, https://doi.org/10.1021/ja306663g.

31. Y. Liang, Y. Jing, S. Gheytani, et al., "Universal Quinone Electrodes For Long Cycle Life Aqueous Rechargeable Batteries," *Nature Materials* 16 (2017): 841–848, https://doi.org/10.1038/nmat4919.

32. X. Liu, Y. Jin, H. Wang, et al., "In Situ Growth of Covalent Organic Framework Nanosheets on Graphene as the Cathode for Long-Life High-Capacity Lithium-Ion Batteries," *Advanced Materials* 34 (2022): 2203605, https://doi.org/10.1002/adma.202203605.

33. W. Zhang, S. Zheng, T. Ma, T. Sun, and Z. Tao, "Hollow Tubular Conjugated Organic Polymer For Lithium Batteries," *Nano Research* 16 (2023): 2474–2479, https://doi.org/10.1007/s12274-022-4995-x.

34. L. Ueberricke, F. Mildner, Y. Wu, et al., "Redox-Active, Porous Pyrene Tetraone Dendritic Polymers As Cathode Materials For Lithium-Ion Batteries," *Materials Advances* 4 (2023): 1604–1611.

35. M. Cheng, S. Zheng, T. Sun, et al., "A Solubility Limited Pyrene-4,5,9,10-Tetraone-Based Covalent Organic Framework For High-Performance Aqueous Zinc-Organic Batteries," *Nano Research* 17 (2024): 5095–5103, https://doi.org/10.1007/s12274-023-6401-8.

36. X. Guo, Q. Yuan, C. Li, et al., "The Synthesis Of Alternating Donor–Acceptor Polymers Based On Pyrene-4, 5, 9, 10-Tetraone And Thiophene Derivatives, Their Composites With Carbon, And Their Lithium Storage Performances As Anode Materials," *RSC Advances* 11 (2021): 15044–15053.

37. X. H. Chen, H. Lu, Z. Wu, et al., "Structure Regulation Induced High Capacity And Ultra-Stable Cycling Of Conjugated Organic Cathodes For Li-Ion Batteries," *Journal of Materials Chemistry A* 11 (2023): 77–83, https://doi.org/10.1039/D2TA08032J.

38. C. J. Yao, Z. Wu, J. Xie, et al., "Two-Dimensional (2D) Covalent Organic Framework as Efficient Cathode for Binder-free Lithium-Ion Battery," *ChemSusChem* 13 (2020): 2457–2463, https://doi.org/10.1002/cssc.201903007.

39. M. Li, J. Liu, Y. Li, et al., "Skeleton Engineering Of Isostructural 2d Covalent Organic Frameworks: Orthoquinone Redox-Active Sites Enhanced Energy Storage," *CCS Chemistry* 3 (2021): 696–706.

40. M. G. Mohamed, S. V. Chaganti, S. U. Sharma, et al., "Constructing Conjugated Microporous Polymers Containing the Pyrene-4,5,9,10-Tetraone Unit for Energy Storage," *ACS Applied Energy Materials* 5 (2022): 10130–10140, https://doi.org/10.1021/acsaem.2c01842.

41. D. Ma, H. Zhao, F. Cao, et al., "A Carbonyl-Rich Covalent Organic Framework As A High-Performance Cathode Material For Aqueous Rechargeable Zinc-Ion Batteries," *Chemical Science* 13 (2022): 2385–2390, https://doi.org/10.1039/D1SC06412F.

42. S. Zheng, D. Shi, D. Yan, et al., "Orthoquinone–Based Covalent Organic Frameworks With Ordered Channel Structures For Ultrahigh Performance Aqueous Zinc–Organic Batteries," *Angewandte Chemie International Edition* 61 (2022): 202117511.

43. H. Gao, A. R. Neale, Q. Zhu, et al., "A Pyrene-4,5,9,10-Tetraone-Based Covalent Organic Framework Delivers High Specific Capacity as a Li-Ion Positive Electrode," *Journal of the American Chemical Society* 144 (2022): 9434–9442, https://doi.org/10.1021/jacs.2c02196.

44. J. Xie, W. Chen, G. Long, et al., "Boosting The Performance Of Organic Cathodes Through Structure Tuning," *Journal of Materials Chemistry A* 6 (2018): 12985–12991, https://doi.org/10.1039/C8TA03857K.

45. Q. Li, D. Li, H. Wang, et al., "Conjugated Carbonyl Polymer-Based Flexible Cathode for Superior Lithium-Organic Batteries," *ACS Applied Materials & Interfaces* 11 (2019): 28801–28808, https://doi.org/10.1021/acsami.9b06437.

46. R. Shi, L. Liu, Y. Lu, et al., "In Situ Polymerized Conjugated Poly (Pyrene-4, 5, 9, 10-Tetraone)/Carbon Nanotubes Composites For

High-Performance Cathode Of Sodium Batteries," *Advanced Energy Materials* 11 (2021): 2002917.

47. H. Pan, Z. Zuo, F. He, and Y. Li, "In-Situ Induced Self-Solidification And Activation Of Ultra-High Energy Density Organic Cathode," *Energy Storage Materials* 52 (2022): 465–472, https://doi.org/10.1016/j.ensm.2022.08.025.

48. F. Adler, S. Pinto-Bautista, C. Lorenz, L. Hinrichs, M. Weil, and B. Esser, "Synthesis of Poly(1,4-anthraquinone) Using Catalytic Amounts of Nickel," *Advanced Science* 12 (2025): 06251, https://doi.org/10.1002/advs.202506251.

49. R. Wessling, K. Chinner, P. Wenz, C. Douglas, O. Dumele, and B. Esser, "Enhanced Solubility and Deprotection of Pyrene-4,5,9,10-tetraones Through Propylene Glycol and Propanediol Protection," *Organic Letters* 27 (2025): 12047–12052, https://doi.org/10.1021/acs.orglett.5c03752.

50. M. B. Minus, S. R. Moor, F. F. Pary, et al., ""Benchtop" Biaryl Coupling Using Pd/Cu Cocatalysis: Application to the Synthesis of Conjugated Polymers," *Organic Letters* 23 (2021): 2873–2877, https://doi.org/10.1021/acs.orglett.1c00479.

51. E. R. Darzi, B. M. White, L. K. Loventhal, L. N. Zakharov, and R. Jasti, "An Operationally Simple and Mild Oxidative Homocoupling of Aryl Boronic Esters To Access Conformationally Constrained Macrocycles," *Journal of the American Chemical Society* 139 (2017): 3106–3114, https://doi.org/10.1021/jacs.6b12658.

52. Z. W. Seh, J. Sun, Y. Sun, and Y. Cui, "A Highly Reversible Room-Temperature Sodium Metal Anode," *ACS Central Science* 1 (2015): 449–455, https://doi.org/10.1021/acscentsci.5b00328.

53. C. Jia, A. Duan, C. Liu, et al., "One-Dimensional Covalent Organic Framework as High-Performance Cathode Materials for Lithium-Ion Batteries," *Small* 19 (2023): 2300518, https://doi.org/10.1002/smll.202300518.

54. D. Sui, L. Xu, H. Zhang, et al., "A 3D Cross-Linked Graphene-Based Honeycomb Carbon Composite With Excellent Confinement Effect Of Organic Cathode Material For Lithium-Ion Batteries," *Carbon* 157 (2020): 656–662, https://doi.org/10.1016/j.carbon.2019.10.106.

55. Z. Sun, M. Shu, J. Li, et al., "Carbon Nanotube-Hyperbranched Polymer Core-Shell Nanowires With Highly Accessible Redox-Active Sites For Fast-Charge Organic Lithium Batteries," *Journal of Energy Chemistry* 78 (2023): 30–36, https://doi.org/10.1016/j.jechem.2022.11.014.

56. H. Wu, S. A. Shevlin, Q. Meng, et al., "Flexible and Binder-Free Organic Cathode for High-Performance Lithium-Ion Batteries," *Advanced Materials* 26 (2014): 3338–3343, https://doi.org/10.1002/adma.201305452.

57. L. Chen, Y. Li, Y. Zhang, et al., "Pyrene-4,5,9,10-Tetraone-Based Covalent Organic Framework/Carbon Nanotube Composite As Sodium-Ion Cathodes With High-Rate Capability," *Chemical Engineering Journal* 497 (2024): 154743, https://doi.org/10.1016/j.cej.2024.154743.

58. M. Tang, S. Zhu, Z. Liu, et al., "Tailoring π-Conjugated Systems: From π-π Stacking to High-Rate-Performance Organic Cathodes," *Chemistry* 4 (2018): 2600–2614, https://doi.org/10.1016/j.chempr.2018.08.014.

59. Z. Wang, Y. Zhang, H. Jiang, et al., "Free-Standing $Na_2C_6O_6$/Mxene Composite Paper For High-Performance Organic Sodium-Ion Batteries," *Nano Research* 16 (2023): 458–465, https://doi.org/10.1007/s12274-022-4696-5.

60. Z. Song, Y. Qian, T. Zhang, M. Otani, and H. Zhou, "Poly(benzoquinonyl sulfide) as a High-Energy Organic Cathode for Rechargeable Li and Na Batteries," *Advanced Science* 2 (2015): 1500124, https://doi.org/10.1002/advs.201500124.

61. J. Liu, P. Lyu, Y. Zhang, P. Nachtigall, and Y. Xu, "New Layered Triazine Framework/Exfoliated 2D Polymer With Superior Sodium-Storage Properties," *Advanced Materials* 30 (2018): 1705401, https://doi.org/10.1002/adma.201705401.

62. Y. Yao, M. Pei, C. Su, et al., "A Small-Molecule Organic Cathode With Extended Conjugation Toward Enhancing Na + Migration Kinetics for Advanced Sodium-Ion Batteries," *Small* 20 (2024): 2401481, https://doi.org/10.1002/smll.202401481.

63. D. Ruiz-Martinez, R. Grieco, M. Liras, N. Patil, and R. Marcilla, "A High Performing Conjugated Microporous Polymer Cathode for Practical Sodium Metal Batteries Using an Ammoniate as Electrolyte," *Advanced Energy Materials* 14 (2024): 2400857, https://doi.org/10.1002/aenm.202400857.

64. M. Adil, A. Sarkar, S. Sau, D. Muthuraj, and S. Mitra, "Non-Aqueous Rechargeable Calcium-Ion Batteries Based On High Voltage Zirconium-Doped Ammonium Vanadium Oxide Cathode," *Journal of Power Sources* 541 (2022): 231669, https://doi.org/10.1016/j.jpowsour.2022.231669.

65. M. Adil, S. Sau, P. Dammala, and S. Mitra, "Comprehensive Study of Sodium Copper Hexacyanoferrate, as a Sodium-Rich Low-Cost Positive Electrode for Sodium-Ion Batteries," *Energy & Fuels* 36 (2022): 7816–7828, https://doi.org/10.1021/acs.energyfuels.2c01043.

66. H. Lindström, S. Södergren, A. Solbrand, et al., "Li^+ Ion Insertion in TiO_2 (Anatase). 2. Voltammetry on Nanoporous Films," *The Journal of Physical Chemistry B* 101 (1997): 7717–7722, https://doi.org/10.1021/jp970490q.

67. V. Augustyn, E. R. White, J. Ko, G. Grüner, B. C. Regan, and B. Dunn, "Lithium-Ion Storage Properties Of Titanium Oxide Nanosheets," *Materials Horizons* 1 (2014): 219–223, https://doi.org/10.1039/C3MH00070B.

68. Z. Xing, Z. Jian, W. Luo, et al., "A Perylene Anhydride Crystal As A Reversible Electrode For K-Ion Batteries," *Energy Storage Materials* 2 (2016): 63–68, https://doi.org/10.1016/j.ensm.2015.12.001.

69. Y. Wang, P. Bai, B. Li, et al., "Ultralong Cycle Life Organic Cathode Enabled by Ether-Based Electrolytes for Sodium-Ion Batteries," *Advanced Energy Materials* 11 (2021): 2101972, https://doi.org/10.1002/aenm.202101972.

70. Y. Hu, Q. Yu, W. Tang, et al., "Ultra-Stable, Ultra-Long-Lifespan and Ultra-High-Rate Na-ion Batteries Using Small-Molecule Organic Cathodes," *Energy Storage Materials* 41 (2021): 738–747, https://doi.org/10.1016/j.ensm.2021.07.008.

Supporting Information

Additional supporting information can be found online in the Supporting Information section.

Supporting File: aenm71098-sup-0001-SuppMat.pdf.